RESEARCH ARTICLE | NOVEMBER 03 2022

Unconventional magnetoresistive behavior near magnetic compensation temperature in ferrimagnetic $Mn_{2.21}Ru_{0.86}Ga$ films

Chunyue Dou; Xiaoguang Xu ✉; Ke Yang; Chexin Li; Tanzhao Zhang; Zhiqiang Zhu; Xiaoyi Zhao; Kangkang Meng; Yong Wu; Jikun Chen; Ming Yang; V. V. Khovaylo; Yong Jiang ✉

Appl. Phys. Lett. 121, 182403 (2022)
https://doi.org/10.1063/5.0123392

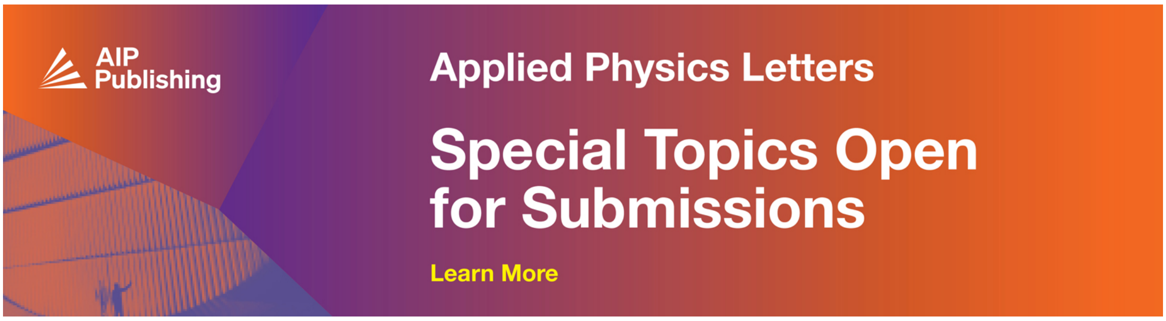

Unconventional magnetoresistive behavior near magnetic compensation temperature in ferrimagnetic $Mn_{2.21}Ru_{0.86}Ga$ films

Cite as: Appl. Phys. Lett. **121**, 182403 (2022); doi: 10.1063/5.0123392
Submitted: 30 August 2022 · Accepted: 7 October 2022 ·
Published Online: 3 November 2022

View Online Export Citation CrossMark

Chunyue Dou,[1] Xiaoguang Xu,[1,a)] Ke Yang,[2] Chexin Li,[1] Tanzhao Zhang,[1] Zhiqiang Zhu,[1] Xiaoyi Zhao,[1] Kangkang Meng,[1] Yong Wu,[1] Jikun Chen,[1] Ming Yang,[2] V. V. Khovaylo,[3] and Yong Jiang[1,a)]

AFFILIATIONS

[1]School of Materials Science and Engineering, University of Science and Technology Beijing, Beijing 100083, China
[2]Department of Applied Physics, The Hong Kong Polytechnic University, Hong Kong, China
[3]National University of Science and Technology MISIS, Moscow 119049, Russia

[a)]**Authors to whom correspondence should be addressed:** xgxu@ustb.edu.cn and yjiang@ustb.edu.cn.
Telephone: +86-10-6233-4698. **Fax:** +86-10-6233-4698

ABSTRACT

Ferrimagnets with magnetic compensation temperature (T_{comp}) around room temperature are desirable due to their potential applications in low-energy consuming and high-frequency spintronic devices. In this study, the T_{comp} of ferrimagnetic $Mn_{2.21}Ru_{0.86}Ga$ (MRG) is tuned to near room temperature by strain. Moreover, we observed unconventional magnetoresistance behaviors for MRG-based Hall bar devices near T_{comp}. First-principles calculations suggest two kinds of Mn moments, which lead to two anomalous Hall channels with opposite signs and consequently correspond to the peak structure and triple loops of the anomalous Hall effect loops. The unconventional temperature dependence of longitudinal resistivity is caused by the combined effects of two types of Mn moments and the anisotropic magnetoresistance of the MRG film. Interestingly, the spontaneous Hall angle of the MRG film is calculated to be ∼2.2%, which is one order of magnitude larger than those of other 3*d* ferromagnets. Therefore, our study demonstrates MRG to be a ferrimagnet with the T_{comp} near room temperature, which enables its potential applications in spintronic devices.

As one branch of the spintronic materials, ferrimagnetic Heusler alloys have attracted increasing attention due to their high spin polarization and low Gilbert damping.[1–3] There are also many other advantages as well, including high-frequency, low power consumption, and high stability of their antiferromagnetic configuration.[1] Recently, Kurt *et al.* have grown a Heusler alloy $Mn_2Ru_{0.5}Ga$ film by co-sputtering and realized the compensated ferrimagnetic half-metal (CFHM) with ordered spin states and zero net magnetic moment.[4] In contrast to standard ferromagnetic metals, CFHMs have no stray magnetic field, which is beneficial to high storage density. Simultaneously, compared to antiferromagnets, CFHMs allow magnetic recording at low power consumption since their magnetic states can be easily switched and detected at the magnetization compensation point.[5] Finley *et al.* have demonstrated that a nearly compensated ferrimagnet ($Mn_2Ru_{0.68}Ga$) can be switched as easily as a conventional ferromagnet.[2] Furthermore, the speed of domain wall motion and spin–orbit torque driven magnetization switching can break the theoretical limits of conventional ferromagnets and reach large values at the compensation temperature or compensation concentration.[6,7] Therefore, the ferrimagnets with magnetic compensation temperature (T_{comp}) around room temperature have potential applications as a fast-flipping free layer in the magnetic recording devices. It has also been reported that T_{comp} is sensitive to the band structure of materials, which makes it possible to tune T_{comp} by adjusting the composition and substrate-induced strain state.[8] Therefore, it is necessary to explore room temperature CFHMs for spintronic applications.

To accelerate the applications of the compensated ferrimagnets in ultrafast and energy-efficient spintronic devices, we report a T_{comp} approaching room temperature in the $Mn_{2.21}Ru_{0.86}Ga$ (MRG) film. Furthermore, we have systematically investigated the anomalous Hall effect (AHE), longitudinal resistivity, and anisotropic magnetoresistance (AMR) of the MRG/Pt heterostructure near the T_{comp}. In order to qualitatively explain the unconventional AHE, we performed first-principles calculations based on the density functional theory (DFT) to reveal the electronics structures and magnetic moment configuration of MRG. In addition, we studied the angle and temperature dependence of the longitudinal resistivity.

MRG films with different thicknesses were grown on MgO (001) substrates by DC co-sputtering of Mn_2Ga and Ru targets. The background pressure was better than 3×10^{-6} Pa. During the sputtering process, the Ar pressure and growth temperature were kept at 0.63 Pa and 500 °C, respectively. The films were annealed *in situ* at 500 °C for 40 min. After cooling to room temperature, Pt (4) or HfO_2 (2) was deposited to protect the MRG films from oxidizing. The surface morphology of the as-deposited MRG films was examined by atomic force microscopy (AFM, BRUKER icon). The crystal structure and thickness of the samples were determined by x-ray diffraction (XRD) and x-ray reflectivity (XRR) on a BRUKER D8 diffractometer, respectively. The hysteresis loops of the samples were measured by a vibrating sample magnetometer (VSM, Quantum Design Versalab). The stacking structure and measurement scheme are illustrated in Fig. 1(a). The AHE, AMR, and longitudinal resistivity were all measured in the physical property measurement system (PPMS, Quantum Design Dyna Cool).

First-principles calculations were performed to achieve optimized geometrical structures and magnetic properties by spin-polarized DFT based Vienna *ab initio* simulation package (VASP) with the projector augmented wave (PAW).[9–11] The generalized gradient approximation (GGA) exchange-correlation functional with Perdew–Burke–Ernzerhof (PBE) format parameter was adopted. A supercell of $Mn_{35}Ru_{13}Ga_{16}$ was constructed via substituting three Ru atoms with three Mn atoms in a $2 \times 2 \times 1$ Mn_2RuGa supercell. The kinetic energy cutoff was set to 350 eV. Γ-centered $9 \times 9 \times 9$ and $5 \times 5 \times 9$ k-points grids were applied for Brillouin zone sampling for the Mn_2RuGa unit cell and $Mn_{35}Ru_{13}Ga_{16}$ supercell, respectively. The convergency criteria for total energy and atomic force were set to 10^{-6} eV and 0.01 eV/Å, respectively. To consider the effect of the lattice strain from the substrate, the lattice constants along x and y axes were constrained, and the lattice constant along the z-axis and all atomic position were fully relaxed. The strain along x and y axes was fixed from −0.02% to 0.03%.

The stoichiometry of as-deposited films is decided to $Mn_{2.21}Ru_{0.86}Ga$ (MRG) by an inductively coupled plasma mass spectrometer. As a full Heusler alloy, the excess Mn atoms will occupy the Ru site in the MRG films.[12] Accordingly, the configuration of $Mn_{35}Ru_{13}Ga_{16}$ ($Mn_{2.19}Ru_{0.81}Ga$) is constructed by substituting three Ru sites with Mn atoms, which is close to the experimental stoichiometry of $Mn_{2.21}Ru_{0.86}Ga$. Then the configuration is optimized by first-principles calculations based on DFT, as shown in Fig. 1(b). The crystal structure of the MRG films with different thicknesses was characterized by XRD. As shown in Fig. 1(c), all the films have obvious (002) and (004) diffraction peaks. The peak position shifted slightly to the right with the thickness. The lattice parameter *c* shrinks from 0.6086 to 0.6065 nm, as shown in the inset of Fig. 1(d). On MgO (001) substrates ($\sqrt{2}a = 0.5956$ nm), the MRG films suffer a compress strain due to the lattice mismatch, resulting in a tetragonal distortion.[2,13] As the film thickness increases, the lattice strain will release, and the lattice parameter *c* decreases toward a cubic crystal structure.[2,13] To verify

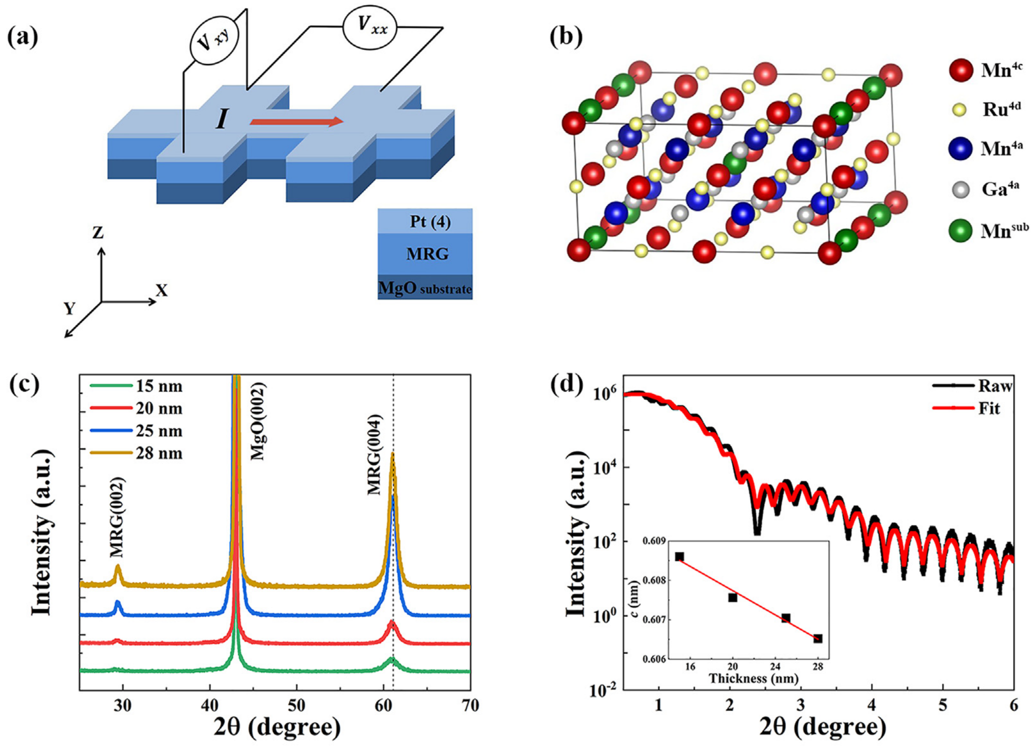

FIG. 1. (a) Schematic illustration of the Hall bar structure and the measurement geometry. (b) The configuration of the $Mn_{35}Ru_{13}Ga_{16}$ supercell. (c) XRD patterns of the MRG films with different thicknesses. (d) XRR pattern of the MRG (28) film together with fitting data. The inset shows the lattice parameter *c* vs the thickness.

the effect of strain on the lattice parameters, we simulated the lattice parameters variation vs the lattice strain by first-principles calculations. As shown in Fig. S1, the out-of-plane lattice parameter c increases gradually with the strain changing from tensile stress to compressive stress, which is consistent with the XRD results. By fitting the XRR data shown in Fig. 1(d), the thicknesses of the films can be determined as 15, 20, 25, and 28 nm. The surface roughness of the MRG (28) film is shown in Fig. S2.

The hysteresis loops of the MRG films with different thicknesses are also shown in Fig. S3. The AHE loops of MRG (t)/Pt (4) heterostructures with different thicknesses were measured at different temperatures. As shown in Figs. 2(a)–2(d), the coercive field ($\mu_0 H_c$) increases first and then gradually decreases with increasing temperature for each MRG thickness. Meanwhile, the sign of R_{xy} reverses at the largest $\mu_0 H_c$ within the experimental temperature region. According to previous studies, the total magnetic moment of a ferrimagnet usually reduces near T_{comp}, and the ferrimagnet requires a large magnetic field to compensate for the magnetic anisotropy energy by obtaining sufficient Zeeman energy.[14] As a result, the ferrimagnet has the largest $\mu_0 H_c$ at T_{comp}.[14,15] Therefore, T_{comp} can be defined in the temperature region with the largest $\mu_0 H_c$ and a reversed sign of R_{xy}. As summarized in Fig. 2(e), the T_{comp} range can be decided according to the AHE loops of the MRG films shown in Fig. 2. It can be found that with the increased thickness, the degree of tetragonal distortion decreases and T_{comp} increases gradually. According to the first-principles calculations as shown in Fig. 2(f), the total magnetic moments (M_T) of $Mn_{32}Ru_{16}Ga_{16}$ and $Mn_{35}Ru_{13}Ga_{16}$ are 17 and 13 μ_B, respectively. In other words, the M_T decreases 4 μ_B by substituting

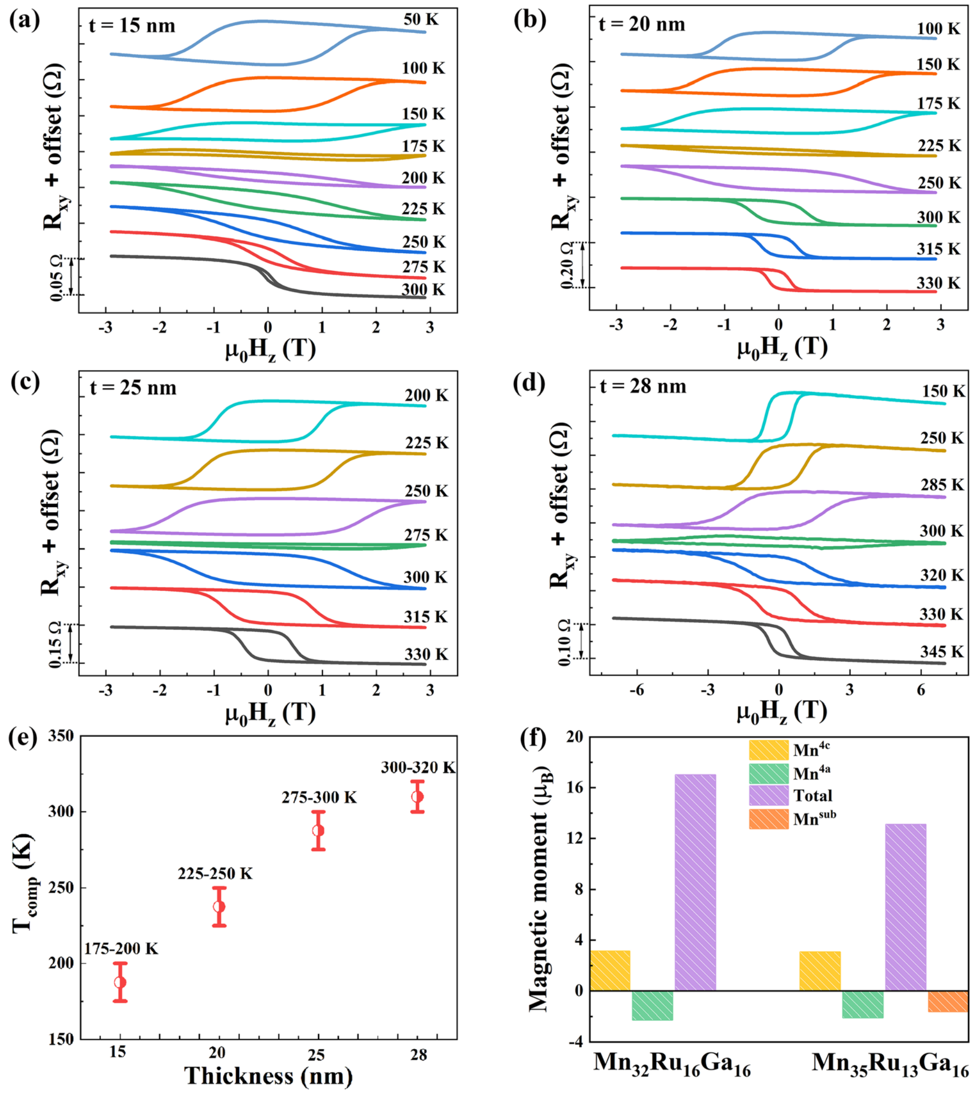

FIG. 2. (a)–(d) The Hall resistance loops of the MRG (t)/Pt (4) heterostructures at different temperatures. (e) T_{comp} dependence on the thickness of the MRG (t)/Pt (4) heterostructures. (f) The comparison of the magnetic moments of $Mn_{32}Ru_{16}Ga_{16}$ (Mn_2RuGa) and $Mn_{35}Ru_{13}Ga_{16}$ ($Mn_{2.19}Ru_{0.81}Ga$).

three Ru sites with Mn atoms. This indicates that occupying of excess Mn atoms in Ru sites will compensate for the M_T. At the same time, strain can also compensate for the M_T (supplementary material Fig. S4). Therefore, the excess Mn atoms and lattice strain are both beneficial to the magnetic compensation. Moreover, the simulation represents the situation at 0 K, and increasing temperature will also facilitate the compensation of magnetic moments.

According to the T_{comp} region for different MRG thicknesses, we chose the MRG (28) film to study the magnetic compensation properties in detail. Figure 3(a) presents the AHE loops measured between 305 and 315 K. The temperature-dependent ΔR_{xy} and $\mu_0 H_c$ are extracted from the AHE loops and shown in Figs. 3(b) and 3(c). Due to $\Delta R_{xy} \approx 0$ and $\mu_0 H_c$ divergence, the T_{comp} of MRG (28) is estimated to be about 308 K.[16,17] Notably, the AHE loops of the MRG film have the peak structure and triple loops near T_{comp}. Generally, this phenomenon might be caused by two-channel AHE or topological Hall effect (THE).[18] However, the THE can be excluded for the following reasons. Above all, the $\mu_0 H_c$ of the MRG films has a maximum at T_{comp}, which is different from the monotonous $\mu_0 H_c$ for a typical THE system.[19–23] In addition, the AHE loops of MRG (28)/HfO$_2$ (2) also have the peak structure and triple loops, and the humps only appear closer to T_{comp} in Fig. S5. However, the humps for the THE exist in a large temperature range.[20,22,23] Therefore, we can exclude the contribution of the THE due to noncoplanar spin textures in the interface between the large spin–orbit coupling element Pt and MRG films. Moreover, the appearance of humps in films without perpendicular magnetic anisotropy (PMA) further rules out the THE contribution since PMA is essential for the formation of skyrmions (supplementary material Fig. S6).[16,24–26]

According to the magnetic moments shown in Fig. 2(f), Mn atoms have a magnetic moment of about $-2\ \mu_B$ in 4a and 4d positions, while have a magnetic moment of about $3\ \mu_B$ in the 4c position. Therefore, the Mn atoms can be classified into Mn$^{\mathrm{I}}$ and Mn$^{\mathrm{II}}$ sites with the magnetic moments of -2 and $3\ \mu_B$, respectively. Based on the calculation results, a schematic model was built to explain the peak structure and triple loops of the MRG (28) sample, as shown in Fig. 3(d). It is reported that the Mn^{4c} magnetization decreases linearly with the increased temperature, and the Mn^{4a} magnetization remains almost constant.[8] Because the magnitude of AHE is proportional to magnetization,[27] the AHE of Mn$^{\mathrm{II}}$ dominates below T_{comp} at which temperature the moments and magnetization of Mn$^{\mathrm{II}}$ outweigh that of Mn$^{\mathrm{I}}$.[8] As shown in Fig. 3(d), the blue (red) loops represent the AHE loops of Mn$^{\mathrm{I}}$ (Mn$^{\mathrm{II}}$), correspondingly to clockwise (anticlockwise) polarity. As the temperature increases, the moments and magnetization of Mn$^{\mathrm{II}}$ gradually weaken, accompanied by the reduced AHE signal. The Mn$^{\mathrm{I}}$ and Mn$^{\mathrm{II}}$ reach equilibrium at $T = T_{comp}$, and ΔR_{xy} approaches zero by the linear superposition of the two AHE loops. At $T > T_{comp}$, the moments and magnetization of Mn$^{\mathrm{II}}$ decrease continuously. As a result, the Hall resistance of Mn$^{\mathrm{I}}$ is larger than that of Mn$^{\mathrm{II}}$. Combining the contributions of Mn$^{\mathrm{I}}$ and Mn$^{\mathrm{II}}$, the total AHE loops take on the peak structure and triple loops near T_{comp}. Therefore, the unconventional AHE evolution with temperature originated from the

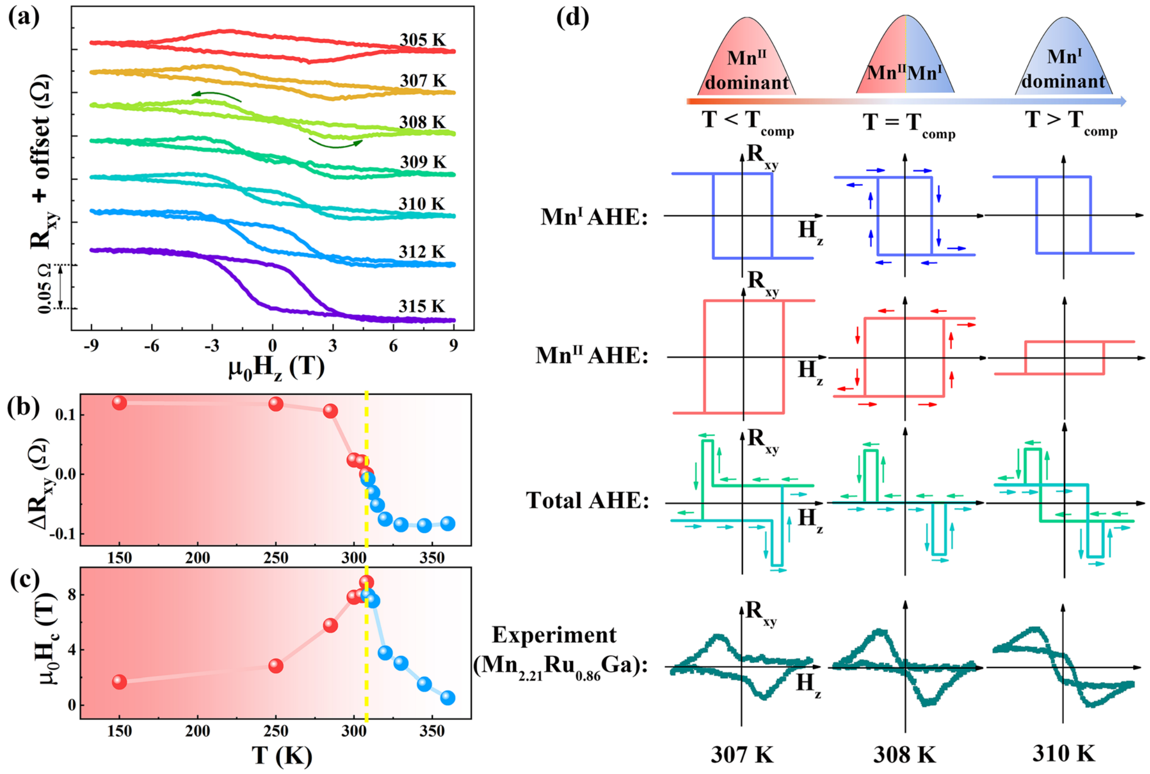

FIG. 3. (a) The AHE loops of the MRG (28)/Pt (4) heterostructure between 305 and 315 K. Temperature dependence of (b) ΔR_{xy} [$\Delta R_{xy} = (R_{xy}^{up} + R_{xy}^{down}/2)$] and (c) the coercive field ($\mu_0 H_c$). (d) Illustration of the peak structure and triple loops by superimposing the AHE channels of two types of Mn moments.

linear superposition of the two AHE loops corresponds to the two sub-lattices with opposite magnetic moments.[16,17]

The longitudinal resistivity can reflect a magnetization state, which is related to T_{comp}. The temperature dependence of the longitudinal resistivity $\Delta\rho_{xx}(\mu_0 H)/\rho_0(\mu_0 H = 0)$ was measured using the MRG (28)/Pt (4) heterostructure as presented in Fig. 4(a). As sweeping the magnetic field, the longitudinal resistivity exhibits bowtie shape loops at $T < T_{comp}$. A similar phenomenon can also be observed in the MRG (28)/HfO$_2$ (2) heterostructure (supplementary material Fig. S7). Figure 4(b) compares the $\Delta\rho_{xx}$ from 0 to 9 T measured at different temperatures. It can be observed that $\Delta\rho_{xx}$ changes from negative to positive with the increased temperature. At the same time, $\Delta\rho_{xx}$ is close to zero within the range of magnetic field at $T = T_{comp}$. The slopes of $\Delta\rho_{xx} - \mu_0 H$ at various temperatures are summarized in Fig. 4(c). The absolute value of the slope decreases with the temperature below T_{comp}. As for a normal magnon magnetoresistance (MMR), the slope should be suppressed due to the reduced magnon number at low temperatures.[28–30] Accordingly, MMR is not the main contribution to the longitudinal resistivity. At the same time, we plot the evolution of spontaneous Hall angle (SHA) with temperature in Fig. 4(d). The SHA increases with temperature and reaches ~2.2% at room temperature, which is about one order of magnitude higher than those of other 3*d* ferromagnets (0.2%–0.3%).[31] Figure 4(e) shows the $\Delta\rho_{xx}/\rho_0$ as a function of the magnetic field at $T = 285$ K and depicts the possible variation of the total magnetic moment with the magnetic field. The Mn^{II} moment is dominant below T_{comp}, so the direction of M_T is consistent with that of the Mn^{II}. Under a magnetic field of +9 T along the z-axis, the Mn^{II} moments point to the +z direction.[32] Therefore, the M_T is parallel to the +z direction. When the magnetic field is further swept to the negative direction, the M_T starts to reverse but not completely.[33] Further increasing the magnetic field over $\mu_0 H_c$, the M_T is reversed completely and aligns in the −z direction.[34] A similar process occurs when the magnetic field sweeps from −9 to +9 T, and the M_T also reverses at $\mu_0 H_c$.

Considering that the AMR has a significant contribution to the longitudinal resistivity, we also studied the AMR of the MRG (28)/Pt (4) heterostructure. As shown in Fig. 5(b), the AMR gradually transforms from positive to negative values with the gradually increasing temperature. To explain the longitudinal resistivity, we exploited Eq. (1) to quantify the AMR contribution, which is based on the mechanism proposed by Park for the study of the ferrimagnet[33]

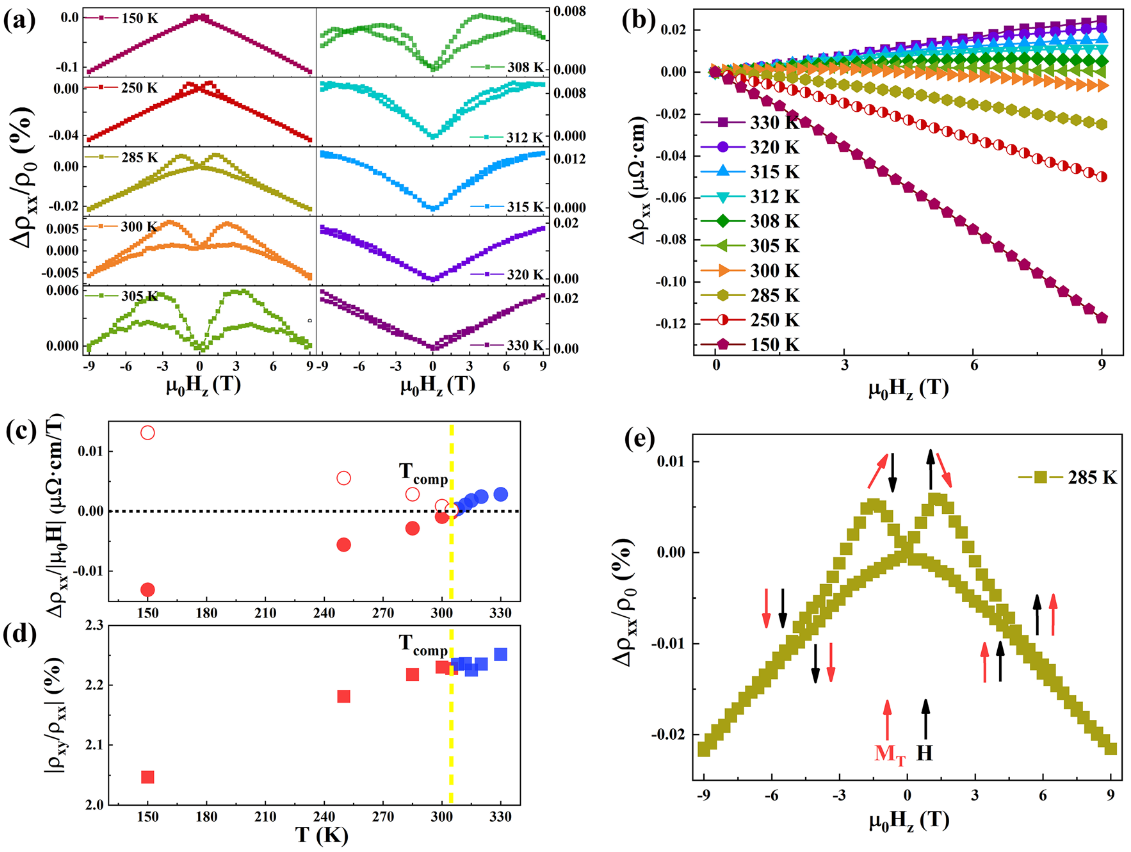

FIG. 4. (a) The variation in $\Delta\rho_{xx}$ as a function of the magnetic field for various temperatures for the MRG (28)/Pt (4) heterostructures. (b) Field-dependent resistivity at different temperatures extracted from (a). (c) The slope of $\Delta\rho_{xx} - \mu_0 H$ extracted from (b). (The solid circle symbols represent the slope. The hollow circle symbols denote the absolute value of the slope for $T < T_{comp}$.) (d) The magnitude of the SHA ($|\rho_{xy}/\rho_{xx}|$) of the MRG (28)/Pt (4) heterostructures as a function of temperature. (e) The variation in $\Delta\rho_{xx}$ as a function of the magnetic field at 285 K for the MRG (28)/Pt (4) heterostructures.

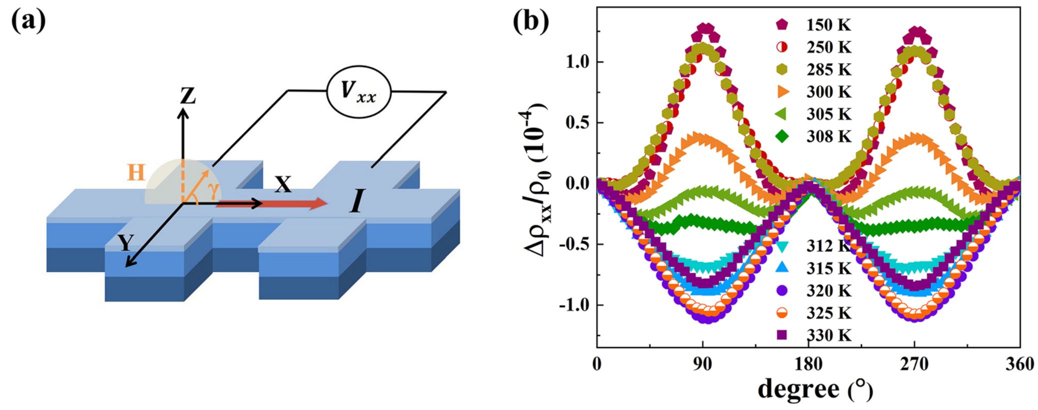

FIG. 5. (a) Schematic diagram of the AMR measurement. (b) AMR curves of the MRG (28)/Pt (4) heterostructures measured under a magnetic field of 9 T at different temperatures.

$$\frac{\partial\rho AMR}{\partial\mu_0 H_z} \approx -A\left\langle m_z^{Mn^I}\right\rangle\left\langle\frac{\partial m_z^{Mn^I}}{\partial\mu_0 H_z}\right\rangle - B\left\langle m_z^{Mn^{II}}\right\rangle\left\langle\frac{\partial m_z^{Mn^{II}}}{\partial\mu_0 H_z}\right\rangle, \quad (1)$$

where $m_z^{Mn^I}$ ($m_z^{Mn^{II}}$) is the z component of the magnetization unit vector of the random $\mathrm{Mn^I}$ ($\mathrm{Mn^{II}}$) site and A (B) represents the magnitude and the sign of AMR of $\mathrm{Mn^I}$ ($\mathrm{Mn^{II}}$). For $T > T_{comp}$ ($T < T_{comp}$), the $\mathrm{Mn^I}$ ($\mathrm{Mn^{II}}$) sub-lattice dominates the total AMR, and the AMR is measured to be negative (positive), from which we can deduce $A < 0$ and $B > 0$. The $\mathrm{Mn^I}$ ($\mathrm{Mn^{II}}$) moments are antiparallel (parallel) to $\mu_0 H_z$ for $T < T_{comp}$;[32] thus, $m_z^{Mn^I} < 0$ and $m_z^{Mn^{II}} > 0$. Since $\frac{\partial m_z^{Mn^I}}{\partial\mu_0 H_z} > 0$ and $\frac{\partial m_z^{Mn^{II}}}{\partial\mu_0 H_z} > 0$, we can conclude $\frac{\partial\rho AMR}{\partial\mu_0 H_z} < 0$, which means a negative slope of $\Delta\rho_{xx}/\mu_0 H$ for $T < T_{comp}$, as shown in Fig. 4(c). Meanwhile, the larger slope of $\Delta\rho_{xx}/\mu_0 H$ at lower temperatures can be explained by the AMR evolution with temperature.[14] Similarly, $m_z^{Mn^I} > 0$ and $m_z^{Mn^{II}} < 0$ for $T > T_{comp}$; thus, the slope of $\Delta\rho_{xx}/\mu_0 H$ is positive. Therefore, both $\mathrm{Mn^I}$ and $\mathrm{Mn^{II}}$ moments dominate the transport properties of the MRG films, including AHE, AMR, and longitudinal resistivity.

Antiferromagnets are immune to the magnetic field, so the experimental study of the antiferromagnetic spin dynamics is always difficult.[15] Our results suggest that MRG can serve as a versatile platform to study nonequilibrium antiferromagnetic transport properties through the interaction of two sub-lattices. In addition, MRG can be tuned to have a T_{comp} around room temperature together with a large SHA, which allows its applications in spintronic devices to achieve the maximum speed of domain wall motion and spin–orbit torque-driven magnetization switching.

In conclusion, the MRG film was optimized to have a room temperature T_{comp}. The transport properties of the ferrimagnetic MRG/Pt heterostructure were systemically studied around T_{comp}. The MRG/Pt heterostructure shows an unconventional AHE caused by the superposition of the two abnormal Hall channels from two kinds of Mn sub-lattices with opposite signs around T_{comp}, which is supported by the first-principles calculations based on DFT. The temperature dependence of longitudinal resistivity shows an inflection point at T_{comp} and a bowtie-like hysteresis phenomenon below T_{comp}, which can be attributed to the combined effects of two types of Mn moments and the AMR of the MRG film. Moreover, the MRG film is demonstrated to have a large SHA of ∼2.2%. Therefore, MRG is a promising ferrimagnetic material with room temperature T_{comp}, which is desirable for future high-frequency and low-energy consumption spintronic devices.

See the supplementary material for more details on the surface morphology, AHE loop, hysteresis loop, and longitudinal resistivity.

This work was partially supported by the Beijing Natural Science Foundation Key Program (Grant No. Z190007), the National Natural Science Foundation of China (Grant Nos. 52061135205, 51971024, 51971027, 51731003, 51971023, and 51927802), and the Russian Science Foundation (Grant No. 21-42-00035).

AUTHOR DECLARATIONS

Conflict of Interest

The authors have no conflicts to disclose.

Author Contributions

Chunyue Dou: Data curation (lead); Formal analysis (lead); Investigation (lead); Writing – original draft (lead); Writing – review and editing (lead). **Xiaoguang Xu:** Funding acquisition (equal); Methodology (lead); Resources (lead); Ke Yang: Data curation (supporting); **Chexin Li:** Investigation (supporting); **Tanzhao Zhang:** Software (supporting); **Zhiqiang Zhu:** Investigation (equal); **Xiaoyi Zhao:** Investigation (equal); **Kangkang Meng:** Visualization (equal); **Yong Wu:** Software (equal); **Jikun Chen:** Software (equal); **Ming Yang:** Methodology (equal); **V. V. Khovaylo:** Investigation (equal); **Yong Jiang:** Project administration (lead).

DATA AVAILABILITY

The data that support the findings of this study are available from the corresponding authors upon reasonable request.

REFERENCES

[1] M. Žic, K. Rode, N. Thiyagarajah, Y.-C. Lau, D. Betto, J. M. D. Coey, S. Sanvito, K. J. O'Shea, C. A. Ferguson, D. A. MacLaren, and T. Archer, Phys. Rev. B **93**, 140202 (2016).

[2] J. Finley, C. Lee, P. Y. Huang, and L. Liu, Adv. Mater. **31**, 1805361 (2019).

[3] G. Bonfiglio, K. Rode, K. Siewerska, J. Besbas, G. Y. P. Atcheson, P. Stamenov, J. M. D. Coey, A. V. Kimel, T. Rasing, and A. Kirilyuk, Phys. Rev. B **100**, 104438 (2019).

[4] H. Kurt, K. Rode, P. Stamenov, M. Venkatesan, Y.-C. Lau, E. Fonda, and J. Coey, Phys. Rev. Lett. **112**, 027201 (2014).

[5] J. Finley and L. Liu, Appl. Phys. Lett. **116**, 110501 (2020).

[6] S. A. Siddiqui, J. Han, J. T. Finley, C. A. Ross, and L. Liu, Phys. Rev. Lett. **121**, 057701 (2018).

[7] K. Cai, Z. Zhu, J. M. Lee, R. Mishra, L. Ren, S. D. Pollard, P. He, G. Liang, K. L. Teo, and H. Yang, Nat. Electron. **3**, 37 (2020).

[8] D. Betto, N. Thiyagarajah, Y.-C. Lau, C. Piamonteze, M.-A. Arrio, P. Stamenov, J. M. D. Coey, and K. Rode, Phys. Rev. B **91**, 094410 (2015).

[9] P. E. Blöchl, Phys. Rev. B **50**, 17953 (1994).

[10] G. Kresse and J. Furthmüller, Phys. Rev. B **54**, 11169 (1996).

[11] G. Kresse and J. Furthmüller, Comput. Mater. Sci. **6**, 15 (1996).

[12] K. E. Siewierska, G. Atcheson, A. Jha, K. Esien, R. Smith, S. Lenne, N. Teichert, J. O'Brien, J. M. D. Coey, P. Stamenov, and K. Rode, Phys. Rev. B **104**, 064414 (2021).

[13] N. Thiyagarajah, Y.-C. Lau, D. Betto, K. Borisov, J. M. D. Coey, P. Stamenov, and K. Rode, Appl. Phys. Lett. **106**, 122402 (2015).

[14] T. Okuno, K.-J. Kim, T. Tono, S. Kim, T. Moriyama, H. Yoshikawa, A. Tsukamoto, and T. Ono, Appl. Phys. Express **9**, 073001 (2016).

[15] K.-J. Kim, S. K. Kim, Y. Hirata, S.-H. Oh, T. Tono, D.-H. Kim, T. Okuno, W. S. Ham, S. Kim, G. Go, Y. Tserkovnyak, A. Tsukamoto, T. Moriyama, K.-J. Lee, and T. Ono, Nat. Mater. **16**, 1187 (2017).

[16] T. Fu, S. Li, X. Feng, Y. Cui, J. Yao, B. Wang, J. Cao, Z. Shi, D. Xue, and X. Fan, Phys. Rev. B **103**, 064432 (2021).

[17] Y. Wang, C. Li, H. Zhou, J. Wang, G. Chai, and C. Jiang, Appl. Phys. Lett. **118**, 071902 (2021).

[18] G. Kimbell, P. M. Sass, B. Woltjes, E. K. Ko, T. W. Noh, W. Wu, and J. W. A. Robinson, Phys. Rev. Mater. **4**, 054414 (2020).

[19] C. Liu, Y. Zang, W. Ruan, Y. Gong, K. He, X. Ma, Q.-K. Xue, and Y. Wang, Phys. Rev. Lett. **119**, 176809 (2017).

[20] Q. Qin, L. Liu, W. Lin, X. Shu, Q. Xie, Z. Lim, C. Li, S. He, G. M. Chow, and J. Chen, Adv. Mater. **31**, 1807008 (2019).

[21] J. Matsuno, N. Ogawa, K. Yasuda, F. Kagawa, W. Koshibae, N. Nagaosa, Y. Tokura, and M. Kawasaki, Sci. Adv. **2**, e1600304 (2016).

[22] B. M. Ludbrook, G. Dubuis, A.-H. Puichaud, B. J. Ruck, and S. Granville, Sci. Rep. **7**, 13620 (2017).

[23] D. Zhao, L. Zhang, I. A. Malik, M. Liao, W. Cui, X. Cai, C. Zheng, L. Li, X. Hu, D. Zhang, J. Zhang, X. Chen, W. Jiang, and Q. Xue, Nano Res. **11**, 3116 (2018).

[24] L. Caretta, M. Mann, F. Büttner, K. Ueda, B. Pfau, C. M. Günther, P. Hessing, A. Churikova, C. Klose, M. Schneider, D. Engel, C. Marcus, D. Bono, K. Bagschik, S. Eisebitt, and G. S. D. Beach, Nat. Nanotechnol. **13**, 1154 (2018).

[25] A. Soumyanarayanan, M. Raju, A. G. Oyarce, A. K. Tan, M.-Y. Im, A. Petrović, P. Ho, K. Khoo, M. Tran, C. Gan, F. Ernult, and C. Panagopoulos, Nat. Mater. **16**, 898 (2017).

[26] W. Jiang, G. Chen, K. Liu, J. Zang, S. G. Te Velthuis, and A. Hoffmann, Phys. Rep. **704**, 1–49 (2017).

[27] N. Nagaosa, J. Sinova, S. Onoda, A. H. MacDonald, and N. P. Ong, Rev. Mod. Phys. **82**, 1539 (2010).

[28] B. Raquet, M. Viret, E. Sondergard, O. Cespedes, and R. Mamy, Phys. Rev. B **66**, 024433 (2002).

[29] V. D. Nguyen, L. Vila, P. Laczkowski, A. Marty, T. Faivre, and J. P. Attané, Phys. Rev. Lett. **107**, 136605 (2011).

[30] A. P. Mihai, J. P. Attané, A. Marty, P. Warin, and Y. Samson, Phys. Rev. B **77**, 060401(R) (2008).

[31] J. W. F. Dorleijn, Philips Res. Repts. **31**, 287 (1976).

[32] C. Fowley, K. Rode, Y.-C. Lau, N. Thiyagarajah, D. Betto, K. Borisov, G. Atcheson, E. Kampert, Z. Wang, Y. Yuan, S. Zhou, J. Lindner, P. Stamenov, J. M. D. Coey, and A. M. Deac, Phys. Rev. B **98**, 220406(R) (2018).

[33] J. Park, Y. Hirata, J.-H. Kang, S. Lee, S. Kim, C. V. Phuoc, J.-R. Jeong, J. Park, S.-Y. Park, Y. Jo, A. Tsukamoto, T. Ono, S. K. Kim, and K.-J. Kim, Phys. Rev. B **103**, 014421 (2021).

[34] J. G. Checkelsky, M. Lee, E. Morosan, R. J. Cava, and N. P. Ong, Phys. Rev. B **77**, 014433 (2008).